CHEMISTRY

Polyoxocationic antimony oxide cluster with acidic protons

Yuki Watanabe[1], Kim Hyeon-Deuk[2], Takafumi Yamamoto[1]†, Masayoshi Yabuuchi[1], Olesia M. Karakulina[3], Yasuto Noda[2], Takuya Kurihara[2], I-Ya Chang[2], Masanobu Higashi[1], Osamu Tomita[1], Cédric Tassel[1], Daichi Kato[1], Jingxin Xia[1], Tatsuhiko Goto[1], Craig M. Brown[4], Yuto Shimoyama[5], Naoki Ogiwara[5], Joke Hadermann[3], Artem M. Abakumov[6], Sayaka Uchida[5]*, Ryu Abe[1,7]*, Hiroshi Kageyama[1,7]*

The success and continued expansion of research on metal-oxo clusters owe largely to their structural richness and wide range of functions. However, while most of them known to date are negatively charged polyoxometalates, there is only a handful of cationic ones, much less functional ones. Here, we show an all-inorganic hydroxyiodide $[H_{10.7}Sb_{32.1}O_{44}][H_{2.1}Sb_{2.1}I_8O_6][Sb_{0.76}I_6]_2{\cdot}25H_2O$ (HSbOI), forming a face-centered cubic structure with cationic $Sb_{32}O_{44}$ clusters and two types of anionic clusters in its interstitial spaces. Although it is submicrometer in size, electron diffraction tomography of HSbOI allowed the construction of the initial structural model, followed by powder Rietveld refinement to reach the final structure. The cationic cluster is characterized by the presence of acidic protons on its surface due to substantial Sb^{3+} deficiencies, which enables HSbOI to serve as an excellent solid acid catalyst. These results open up a frontier for the exploration and functionalization of cationic metal-oxo clusters containing heavy main group elements.

INTRODUCTION

Polyoxometalates (POMs) are anionic metal oxide clusters consisting of interconnected metal-oxygen polyhedral units, which are present in a solution or as a crystalline solid when combined with counter ions (*1*, *2*). Since its first discovery in the 1800s, a large variety of negatively charged POMs has been found, including Lindqvist type $[M_6O_{19}]^{n-}$ (M = Mo, W, V, etc.), Anderson type $[H_x(M'O_6)M_6O_{18}]^{n-}$, Keggin type $[XM_{12}O_{40}]^{n-}$ (X = S, P, Si, etc.), and Wells-Dawson type $[X_2M_{18}O_{62}]^{n-}$, to name only a few. In addition to the compositional diversity of each POM, the intrinsic isomerism and ability to form lacunary and substituted structures further increase the structural diversity and expand the reaction possibilities (*3*). The resulting structures permit a wide range of chemical and physical properties such as homo- and heterogeneous catalysis (*4*, *5*), selective ion capturing (*6*), and biochemical applications (*7*) arising from the redox activity of transition metals in POMs, as well as quantum computing (*8*).

Contrary to the negatively charged POMs, positively charged metal-oxo clusters (metal-oxo polycations) are quite rare (*9*, *10*), but in recent years, special attention has been paid to the development of the synthesis of cationic metal-oxo clusters (*11*–*15*), such as $[Al_{13}O_4(OH)_{24}(H_2O)_{12}]^{7+}$ (Al_{13}) (*16*), $[Dy_2(H_2O)_8V_{12}O_{32}]^{2+}$ (*17*), and $[Zr_{25}O_{10}(OH)_{50}(O_2)_5(H_2O)_{40}]^{8+}$ (*18*, *19*), and isolation of these clusters. While applications ranging from water purification to catalysis have been searched for Al_{13} and its analogs (*20*–*22*), the research on cationic metal-oxo clusters, in general, is in its infancy, and most studies focus on the synthetic and structural aspects, while their functions remain practically unexplored. Thus, the finding of a previously unknown cationic metal-oxo clusters not only provides a structural impact of its own but also promises unique functions in a solution or as various complexes when combined with negatively charged counter anions.

In this study, we report on $[H_{10.7}Sb_{32.1}O_{44}][H_{2.1}Sb_{2.1}I_8O_6][Sb_{0.76}I_6]_2{\cdot}25H_2O$ (**HSbOI**) serendipitously found during the search for an antimony oxyiodide for photocatalytic applications. This product has cationic clusters of $[H_{10.7}Sb_{32.1}O_{44}]^{19.0+}$ (**HSbO**) that form a face-centered cubic (fcc) packed lattice with $[H_{2.1}Sb_{2.1}I_8O_6]^{11.6-}$ and $[Sb_{0.76}I_6]^{3.7-}$ clusters at the interstitial sites (Fig. 1A). Unlike the structurally related $Sb_{35}O_{44}X_5$ cluster in $Cu_{20}Sb_{35}O_{44}X_{37}$ (X = Cl, Br) (*11*, *23*), the cationic cluster in **HSbOI** carries protons, of which the surface protons are acidic, achieving excellent activity in heterogeneous acid-catalyzed reactions. Thus, this study opens a frontier in the study of metal-oxo clusters as solid catalysts, which has so far been limited to anionic transition metal oxide clusters.

RESULTS AND DISCUSSION

Synthesis and structural characterization of HSbOI

HSbOI was obtained by accident in an attempt to prepare an unreported $Sb_4O_5I_2$, which we expected to be isostructural with $Sb_4O_5Cl_2$ and $Sb_4O_5Br_2$ (*24*), but has a smaller bandgap, using a solution process suitable for solar cell applications. This oxyiodide (Fig. 2C, bright orange, and fig. S1) was obtained by dissolving antimony oxide in an aqueous hydrogen iodide solution at room temperature (RT), followed by dilution with water. The powder synchrotron x-ray diffraction (SXRD) pattern (Fig. 2C) differs markedly from the expected pattern for the monoclinic $Sb_4O_5Cl_2$ structure, with numerous peaks at low angles that prevented us from even determining the unit cell.

[1]Department of Energy and Hydrocarbon Chemistry, Graduate school of Engineering, Kyoto University, Nishikyo-ku, Kyoto 615-8510, Japan. [2]Division of Chemistry, Graduate School of Science, Kyoto University, Kyoto 606-8502, Japan. [3]EMAT, University of Antwerp, 2020 Antwerpen, Belgium. [4]Center for Neutron Research, National Institute of Standards and Technology, Gaithersburg, MD 20899, USA. [5]Department of Basic Science, School of Arts and Sciences, The University of Tokyo, Meguro-ku, Tokyo 153-8902, Japan. [6]CEST, Skolkovo Institute of Science and Technology, 121205 Moscow, Russia. [7]CREST, Japan Science and Technology Agency (JST), Kawaguchi, Saitama 332-0012, Japan.
*Corresponding author. Email: kage@scl.kyoto-u.ac.jp (H.K.); ryu-abe@scl.kyoto-u.ac.jp (R.A.); csayaka@g.ecc.u-tokyo.ac.jp (S.U.)
†Present address: Tokyo Institute of Technology, Yokohama 226-8503, Japan.

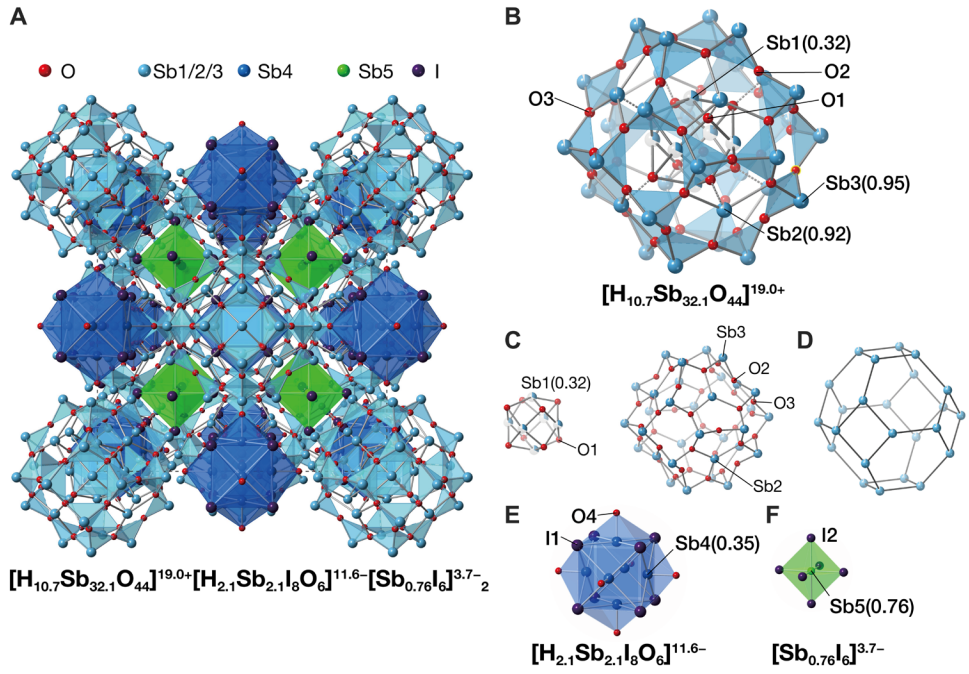

Fig. 1. Structure of dehydrated $[H_{10.7}Sb_{32.1}O_{44}][H_{2.1}Sb_{2.1}I_8O_6][Sb_{0.76}I_6]_2$. (**A**) Dehydrated **HSbOI** [*Fm*-3*m*, $a = 21.3305(1)$ Å]. Red and purple spheres, respectively, represent O and I atoms, while light blue, blue, and green spheres represent Sb1/2/3, Sb4, and Sb5, respectively. Cationic clusters **HSbO** form an fcc lattice with the anionic clusters $[H_{2.1}Sb_{2.1}I_8O_6]^{11.6-}$ and $[Sb_{0.76}I_6]^{3.7-}$ at the octahedral and tetrahedral interstitial sites, respectively (see also fig. S7, A and B). (**B**) A large cluster **HSbO**. (**C**) The **HSbO** cluster is composed of (left) the inner shell $[Sb1_{6-\delta}O_8]$ ($\delta \sim 4$) and (right) the outer shell $[Sb_{32-\delta}O_{36}]$ ($\delta \sim 2$) {or $[Sb2_{8-\delta}(Sb3_{24-\delta'}O_{36})]$ ($\delta \sim 0.8$, $\delta' \sim 1.2$)}. The outer shell contains a $[Sb3_{24-\delta}O_{36}]$ ($\delta \sim 1$) cage with eight $[Sb2_{1-\delta}]$ cations ($\delta \sim 0.1$). The inner and outer shells are connected through Sb2—O1 [dashed bond in (B)]. For simplicity, the Sb2-site (32*f*) splitting into 96*k* is omitted in (A) to (C) (see fig. S7C for the structure with the Sb2-site splitting). (**D**) The $[Sb3_{24-\delta}O_{36}]$ cage with sodalite 4^66^8 topology. (**E**) A medium cluster $[H_{2.1}Sb_{2.1}I_8O_6]^{11.54-}$. (**F**) A small cluster $[Sb_{0.76}I_6]^{3.7-}$.

Because of its particle size of <200 nm (fig. S2), to resolve the crystal structure, we used three-dimensional electron diffraction (3D-ED) tomography, a powerful technique that allows to determine structures from submicrometer single crystals and has recently been applied to a variety of materials from metal oxide to proteins (*25*–*27*), but not to metal-oxo cluster compounds. The combination of selected area ED patterns (Fig. 2A, fig. S3, and table S1), high-resolution high-angle annular dark-field scanning transmission electron microscopy (HAADF-STEM) images (Fig. 2B and fig. S4), and structure solution from 3D-ED data using charge flipping methods provides the initial structure model in the cubic *Fm*-3*m* space group with a large lattice parameter $a = 21.3305(1)$ Å (details in the Supplementary Materials). The 3D-ED analysis revealed large pseudo-spherical $Sb_{38-\delta}O_{36}$ clusters with a diameter of ~13 Å (fig. S5A), assembled in an fcc packed lattice. Subsequent Rietveld refinement from the powder SXRD data (Fig. 2C) revealed additional oxygens in the large clusters and the presence of small- and medium-sized clusters. There are considerable amounts of Sb vacancies in each cluster type, with average compositions of $Sb_{38-\delta}O_{44}$ [$\delta = 5.95(5)$], $Sb_{6-\delta}I_8O_6$ [$\delta = 3.89(3)$], and $Sb_{1-\delta}I_6$ [$\delta = 0.241(5)$] for the large, medium, and small clusters, respectively (table S2).

The chemical composition of $[Sb_{32.1}O_{44}]^{8.3+}[Sb_{2.1}I_8O_6]^{13.7-}[Sb_{0.76}I_6]^{3.7-}{}_2$ estimated above is not charge-neutral, but the presence of substantial amounts of protons is suggested by the intense background of a neutron powder diffraction profile originating from the incoherent scattering on hydrogen (fig. S11). To maintain charge neutrality, 12.8 protons should be present per formula unit. As discussed later, magic angle spinning nuclear magnetic resonance (MAS-NMR) experiments and ab initio calculations demonstrate that protons bind to the large and medium clusters, together with water of crystallization (fig. S12). Assuming that each cluster takes on two specific compositions around the average H or Sb value, the final formula can be given by $[(\{(H_5Sb1_2O_8)_{0.5}(H_6Sb1_2O_8)_{0.5}\}_{0.92}\{(H_5Sb1_1O_8)_{0.5}(H_6Sb1_1O_8)_{0.5}\}_{0.08})\cdot(Sb2_7)_{0.6}(Sb2_8)_{0.4}\cdot(\{(H_5Sb3_{23}O_{36})_{0.8}(H_6Sb3_{23}O_{36})_{0.2}\}_{0.8}\{(H_5Sb3_{22}O_{36})_{0.8}(H_6Sb3_{22}O_{36})_{0.2}\}_{0.2})]\cdot[\{(H_2Sb4_3I_8O_6)_{0.9}(H_3Sb4_3I_8O_6)_{0.1}\}_{0.1}\{(H_2Sb4_2I_8O_6)_{0.9}(H_3Sb4_2I_8O_6)_{0.1}\}_{0.9}]\cdot[(I_6)_{0.24}(Sb5I_6)_{0.76}]_2\cdot 25H_2O$. Unless otherwise stated, we will hereafter use a simplified chemical formula of $[H_{10.7}Sb_{32.1}O_{44}][H_{2.1}Sb_{2.1}I_8O_6][Sb_{0.76}I_6]_2\cdot 25H_2O$ (**HSbOI**). As displayed in Fig. 1A, the octahedral and tetrahedral voids in the positively charged clusters of **HSbO** in the fcc structure are occupied by medium and small anionic clusters, respectively.

Structural features of clusters in HSbOI

The **HSbO** cluster $[Sb_{32.1}O_{44}]^{8.3+}$ ($Sb_{38-\delta}O_{44}$, where $\delta \sim 6$) consists of an $Sb_{32-\delta}O_{36}$ ($\delta \sim 2$) outer shell and an $Sb_{6-\delta}O_8$ ($\delta \sim 4$) inner shell (Fig. 1B). The outer shell is composed of a $[Sb_{24-\delta}O_{36}]$ cage and eight $[Sb_{1-\delta}]$ cations (Fig. 1, B and C, and fig. S7c). The $[Sb_{24-\delta}O_{36}]$ cage contains the Sb_{24} framework with truncated octahedron of 4^66^8 geometry (Fig. 1D), which is also seen in other compounds (*28*–*30*), as discussed later. The outer shell Sb^{3+} (Sb2 and Sb3) cations are strongly asymmetric, with a triangular oxygen environment (SbO_3E), where Sb 5s lone electron pair (E) is pointing outward, thereby stabilizing the cluster structure, which is theoretically validated as shown in Fig. 3A. A similar $Sb_{38-\delta}O_{44}$ cluster is found in $Cu_{20}Sb_{35}O_{44}X_{37}$ (X = Cl, Br) (fig. S6), where the cluster appears to be

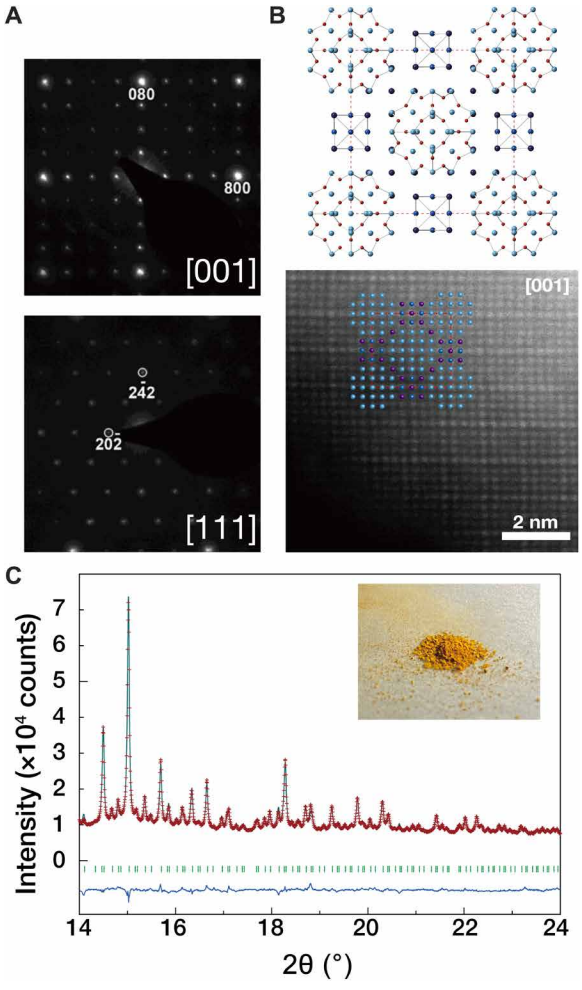

Fig. 2. ED and XRD patterns of $[H_{10.7}Sb_{32.1}O_{44}][H_{2.1}Sb_{2.1}I_8O_6][Sb_{0.76}I_6]_2{\cdot}25H_2O$ (HSbOI). (**A**) The ED patterns of **HSbOI** along [001] and [101] (see fig. S3 for details). (**B**) Structure model obtained by ED tomography and high-angle annular dark-field scanning transmission electron microscopy (HAADF-STEM) image of **HSbOI**, where red, blue, and purple balls represent O, Sb, and I atoms, respectively. Note that STEM measurement does not distinguish between antimony ($Z = 51$) and iodide ($Z = 53$). (**C**) Rietveld refinement of SXRD pattern [$\lambda = 0.42096(1)$ Å] in the region of 14° to 24° (see fig. S8 for the full data). Red overlying crosses and green solid curve represent the observed and the calculated intensities, respectively. The bottom stands for the residual curve. The inset is a photo of bright orange powder of **HSbOI**.

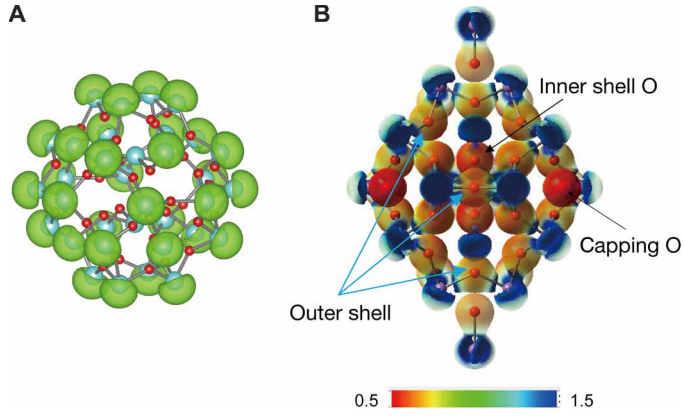

Fig. 3. Calculated large cluster of HSbO polycation. (**A**) Lone-pair orbitals of the outer shell Sb atoms for $[Sb_{34}O_{44}]^{14+}$, which consists of defect-free outer shell $[Sb_8(Sb_{24}O_{36})]$ and $[Sb_2O_8]$ inner shell taking into account large Sb1 vacancies (see Materials and Methods), with the isovalue of 0.1 for orbital plotting. (**B**) 3D electrostatic potential (ESP) maps calculated from the 3D density functional theory (DFT)–optimized wave function of the extended cluster of $[Sb_{36}O_{50}]^{8+}$, where capping O—Sb (× 2) and O—V_{Sb} (× 4) originated from the neighboring medium $Sb_{6-\delta}I_8O_6$ clusters (where V_{Sb} represents an antimony vacancy) are added to the $[Sb_{34}O_{44}]^{14+}$ cluster. All the oxygen sites show smaller ESPs (red), which attract positively charged protons (see also fig. S20). In contrast, all the antimony sites show larger ESP values (blue). The value of ESP decreases in the order of oxygen at the outer shell, inner shell, and capped O—Sb, meaning that the outer shell oxygen is the least weakly bound to protons and is easiest to release them. Each figure is visualized using the VESTA program (*60*).

stabilized by sheets of CuX_4 tetrahedra (*11*, *23*), whereas the **HSbO** cluster is ionically stabilized with two types of anionic clusters. Another difference is that $Cu_{20}Sb_{35}O_{44}X_{37}$ is prepared using a solid-state reaction at 500°C in vacuum, so there are no protons present.

The medium $[Sb_{2.1}I_8O_6]^{13.7-}$ cluster (Fig. 1E) resembles the face-capped $M_6Ch_8X_6$ units of the well-known Chevrel-type compounds with transition metals (M = Mo, Re,…; Ch = S, Se,…; X = Cl, PEt_3,…) (*31*). The formation of Chevrel-type clusters can be interpreted in terms of electronic stabilization, where the highest occupied molecular orbitals are mainly of metal-metal bonding nature. In contrast, the d orbitals of Sb^{3+} ion in $Sb_{6-\delta}I_8O_6$ are fully occupied ($4d^{10}$), indicating that this medium cluster is not stable by itself but is somehow stabilized by the "nanospace" formed by the fcc network of **HSbO** clusters through covalent interactions. The O^{2-} ions in $Sb_{6-\delta}I_8O_6$ bind not only to Sb4 within this cluster but also to Sb3 in the **HSbO** cluster, indicating a substantial interaction between the two clusters, which is supported by bond valence sum (BVS) calculations (see Supplementary Text). Thus, the six Sb4 ions appear to be assembled merely to orient the Sb 5s orbitals toward the octahedral center. Such "clustering" of cations with lone-pair electrons has been observed in solids with Sb, Bi, Pb, and Te (*32*).

The small $[Sb_{0.76}I_6]^{3.7-}$ cluster (Fig. 1F) is also unusual because the Sb deficiency (24%) implies a cation-vacant $(I_6)^{6-}$ octahedron. For inorganic molecules and metal complexes, MX_6 octahedra (e.g., $[Fe(CN)_6]^{3-}$ and $[SiF_6]^{2-}$) do not permit a metal deficiency without being accompanied by a ligand defect (*33*). The situation differs markedly from extended oxides such as perovskite oxides where octahedral metal defects are often seen (*34*). The strong interaction with the **HSbO** cluster is once again expected to stabilize this cluster; when only the octahedral center (Sb5) is considered, the BVS value of I2 is as small as −0.44, but it rises to −0.86 when Sb2 and Sb3 sites of the large cluster are included.

Acidic protons and catalysis

^1H MAS-NMR profile of the dehydrated **HSbOI** was collected to obtain information about the states of protons. As shown in Fig. 4A, the spectrum mainly consists of three peaks centered at 10, 6, and 4.5 parts per million (ppm) with a peak area ratio of about 25:10:26 (see fig. S13 for the spectrum of the as-prepared sample). We computationally determined the stable proton positions for an extended cluster of $[Sb_{36}O_{50}]^{8+}$ that has a large cluster {consisting of outer $[Sb2_8(Sb3_{24}O_{36})]$ and inner $[Sb1_2O_8]$} taking into account Sb vacancies, plus two capping [O—Sb4] and four [O—V_{Sb}] units of the middle cluster $[Sb4_{6-\delta}I_8O_6]$ (where V_{Sb} represents an antimony vacancy).

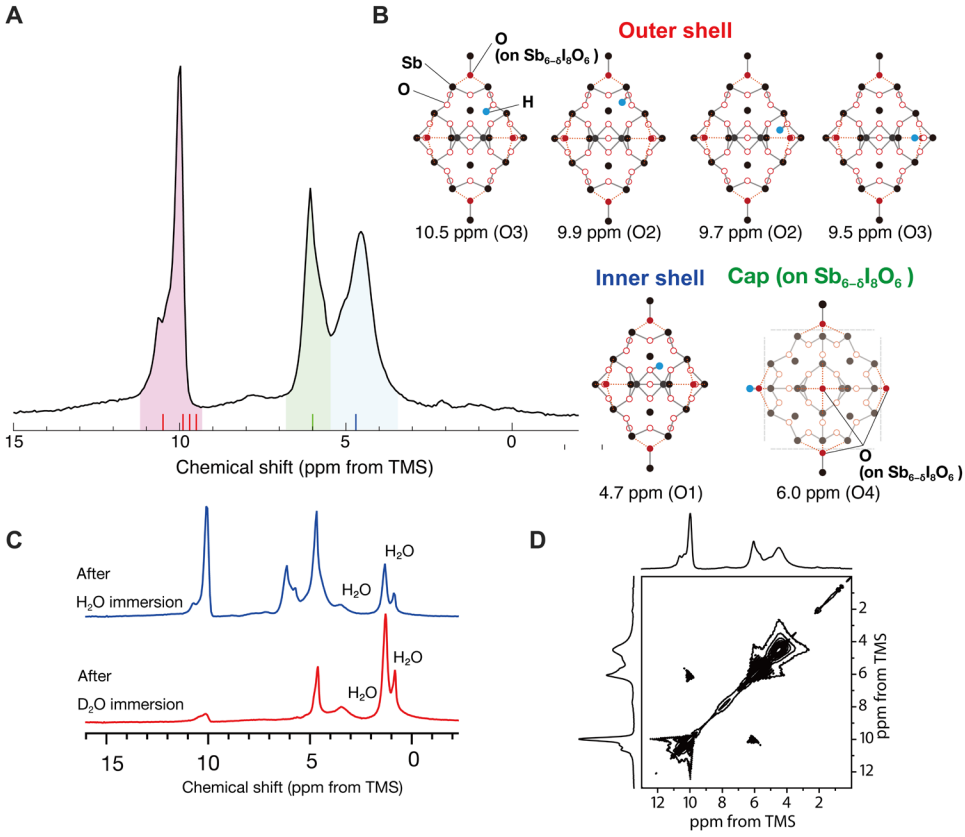

Fig. 4. ^{1}H MAS-NMR data of HSbOI. (**A**) An RT ^{1}H MAS-NMR spectrum of dehydrated **HSbOI** with calculated chemical shifts, where red, green, and blue bars denote protons attached to O2 and O3 in the outer shell, capped O4, and O1 in the inner shell, respectively. Three peaks centered at 10 ppm (outer shell), 6 ppm (cap), and 4.5 ppm (inner shell) have the area intensity ratio of about 25:10:26. Note that this ratio is a rough estimate because there is a small peak around 4.5 ppm (and 1 to 3 ppm) attributed to residual hydrated water (fig. S12). (**B**) Optimized structures and NMR chemical shifts of an extended $[HSb_{36}O_{50}]^{9+}$ cluster, where the proton (light blue circle) is attached to O2 or O3 (open red circle) in the outer shell, to O1 (open red circle) in the inner shell, and to the capped O4 (filled red circle) (fig. S19). Black circles represent Sb atoms. The oxygen in the position overlapping the proton is omitted. (**C**) ^{1}H NMR spectrum of the samples after immersing the as-prepared one in H_2O (blue) and in D_2O (red). The disappeared signals at 10 and 6 ppm after D_2O immersion indicate H/D exchange, supporting our computational assignment of proton adsorption in the outer shell and capped oxygen. (**D**) A contour plot obtained by covariance processing a 2D ^{1}H RFDR NMR spectrum of dehydrated **HSbOI** with a mixing time of 1.6 ms. A 2D ^{1}H RFDR spectrum recouples the homonuclear dipolar couplings depending on the nuclear distance. Therefore, the cross peak between 6 and 10 ppm means that protons corresponding to each chemical shift are close in distance.

The density functional theory (DFT) and the gauge-independent atomic orbital (GIAO) method were used to compute chemical shifts (see the "Computational methods" section). The extended $[Sb_{36}O_{50}]^{8+}$ structure was fixed as the experimentally determined one, while the position of an added proton was fully optimized. As shown in Fig. 4B, there are roughly three stable H^+ positions at 9.5 to 10.5 ppm for H^+ bound to O2 and O3 in the outer shell, 4.7 ppm for H^+ bound to O4 in the inner shell, and 6.0 ppm for H^+ bound to the capped O1. These calculated chemical shifts reproduced the experimental data extremely well. The ^{1}H MAS-NMR spectrum after soaking in heavy water (Fig. 4C) supports the 10-ppm signal being assigned to protons on the surface of large clusters. Moreover, a 2D ^{1}H radio frequency–driven recoupling (RFDR) NMR spectrum (Fig. 4D), which recouples the homonuclear dipolar couplings depending on the nuclear distance, further validates the aforementioned computational assignment because the observed cross peak between 6 and 10 ppm means that protons corresponding to each chemical shift are close in distance.

The relationship between ^{1}H MAS-NMR chemical shift and acidity has been well known both experimentally (*35*) and theoretically (*36*); the larger the chemical shift in solid-state NMR, the higher the acidity. For instance, the silanol groups of zeolites (H-mordenite) exhibit ^{1}H MAS-NMR chemical shifts of ca. 2 ppm (*37*), while those of the Brønsted acid sites of zeolites (H-mordenite) (*37*) and acidic Nafion (*38*) are observed at ca. 4 and 9.7 ppm, respectively. The chemical shift of the protons in the outer shell (10 ppm) of the **HSbO** cluster is as large as those of the typical acidic salts of Keggin-type POM (*39*) and the acidic polymer of Nafions (*38*), suggesting that the surface of the **HSbO** cluster in **HSbOI** must be acidic.

In expectation of the high catalytic activity of the **HSbO** surface as a Brønsted acid, we carried out pinacol rearrangement reaction, which is a typical acid-catalyzed reaction (*40*). In the pinacol rearrangement reaction, elimination of water from pinacol (a diol) gives pinacolone (a ketone) via 1,2-methyl shift as a major product and 2,3-dimethyl-1,3-butadiene (an olefin) via simple dehydration as a minor product (*40*). As shown in Fig. 5A, **HSbOI** exhibits high catalytic activity as a solid catalyst (entry 1, 100% conversion and >99% selectivity to pinacolone) at 373 K and 1 hour in toluene [see figs. S14 and S15 for the ^{1}H NMR and gas chromatography (GC) chart, respectively]. The catalytic performance of **HSbOI** is comparable to

A Pinacol rearrangement reaction

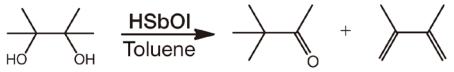

Entry	Catalyst	Amount of catalyst (mmol/mg)	Surface area of catalyst ($m^2 g^{-1}$)	Conversion (%)	Yield (%)
1	**HSbOI**	0.01/300*	8	100	>99
2	**Cs2.5**	0.01/118	150	100	93†

B Barbier-Grignard reaction

Entry	HSbOI (μmol)	Time (hours)	Yield (%)	Turnover number	Turnover frequency ($hour^{-1}$)
1	0.5	1	5.0	50	50
2	0.5	24	22	220	9.2
3	1.0	1	6.3	31.5	31.5
4	1.0	24	63	315	13

Fig. 5. Catalytic reaction with HSbOI. The result of (**A**) pinacol rearrangement reaction in toluene and (**B**) Barbier-Grignard reaction in aqueous media. TON and TOF were calculated from the equation TON = [yield (%)]/[amount of catalyst (mol)/amount of substrate (mol)] and TOF ($hour^{-1}$) = TON/reaction time (hours). Asterisk indicates that 300 mg of **HSbOI** corresponds to 0.01 mmol based on its unit cell ($Z = 4$). Note that the amounts of metal-oxo clusters (**HSbO** or $[PW_{12}O_{40}]^{3-}$) are the same in entries 1 and 2. Dagger indicates that no other products were detected in entry 2 (2,3-dimethyl-1,3-butadiene was not detected). Unidentified peaks at long retention times were observed in the GC chart of the reaction solution of entry 2.

those of Keggin-type heteropolyacids (100% conversion and 43 to 78% selectivity to pinacolone at 423 K and 1 hour), which are well-known superacids (*41*). The reaction under the same conditions using the well-known POM-based solid acid catalyst $Cs_{2.5}H_{0.5}PW_{12}O_{40}$ (**Cs2.5**) (*42*) showed 100% conversion of pinacol and 93% selectivity to pinacolone, demonstrating that the performance of **HSbOI** is comparable. The powder XRD pattern of **HSbOI** after the reaction is analogous to that before the reaction (fig. S16), showing that the crystal structure of the catalyst is maintained during the reaction. As shown in Fig. 5A, **HSbOI** can be easily recovered from the reaction mixture by simple filtration and washing with toluene and can be reused at least once (entry 2, 100% conversion and >92% selectivity to pinacolone).

In addition, we carried out allylation of aldehydes using the Barbier-Grignard reaction, which is a typical acid-catalyzed reaction in water and an environmentally friendly C—C bond formation method (*43*). Figure 5B lists the results of the Barbier-Grignard reaction catalyzed by **HSbOI**; 1-phenyl-3-butene-1-ol was identified as the sole reaction product of this reaction by GC and ^{1}H NMR. Removing the catalyst stopped the reaction, indicating that the observed catalysis is truly heterogeneous (fig. S17). Elemental analysis of the reaction solution by inductively coupled plasma mass spectrometry (ICP-MS) showed that the amount of Sb that leached from **HSbOI** after 24 hours was ca. 0.4% and negligible. The yield and turnover number (TON) with 0.2 mole percent (mol %) of **HSbOI** (based on benzaldehyde) in H_2O at 353 K and 24 hours were 63% and 315, respectively. Notably, the turnover frequency (TOF) reached a high value of 50 per hour with 0.1 mol % of **HSbOI** at 1 hour, which is higher than that of a typical solid acid catalyst, a scandium triflate–grated mesoporous silica (TON ~ 200 and TOF < 1 at 353 K) (*44*). It is known that the activity in the Barbier-Grignard reaction increases by increasing the acid strength of POM-based solids as catalysts [i.e., pK_a (where K_a is the acid dissociation constant) of the metal aqua ions as counter cations] (*45*), so these results confirm the highly acidic property of **HSbOI**. Because **HSbOI** is not porous (fig. S18), the activity per proton is high, given that the reaction with benzaldehyde in this case occurred only on the small surface of **HSbOI** particles. We note that no by-products due to the redox property of iodine were observed in both reactions.

While metal-oxo cluster materials have been extensively studied as catalysts for a variety of acid-base and redox reactions (*4*, *5*, *46*), most of the clusters are composed of transition metals and/or light main group metals. In this regard, **HSbOI** composed of late main group elements (Sb) is unprecedented in demonstrating excellent properties as a solid acid. In addition to the large chemical shift, the unusually weak binding of the protons in the large cluster's surface (attached to O2 or O3) can be presumed from the computed O—H bond length of 1.013 to 1.045 Å, which is longer than 1.010 Å for O1—H and 0.979 Å for O4—H) (fig. S19). To obtain further insights into the bonding nature of H^+, we calculated electrostatic potentials (ESPs) (*47*). Figure 3B shows that the DFT-optimized ESPs of the extended $[Sb_{36}O_{50}]^{8+}$ cluster increase in the order of outer shell oxygen, inner shell oxygen, and capped oxygen. The reason for the presence of acidic protons attached to the outer shell is not immediately available but is speculated to be as follows. A large number of vacancies are created in the inner shell to relieve the overbonding of antimony sites (Sb1), which, in turn, generate a large number of charge balancing protons (three H^+ for each Sb^{3+} defect). However, because there are only a limited number of oxygen sites (O1) in the inner shell that can bond more strongly with hydrogen than oxygen sites of the outer shell, the extra protons should bond to oxygen of the outer shell, resulting in high Brønsted acidity. In addition, the stereochemically active lone-pair electrons of the **HSbO** surface (Fig. 3A) may somehow contribute to the reaction process.

Outlook

We have successfully synthesized an all-inorganic hydroxyiodide containing a large cationic antimony-based cluster, featuring acidic protons. Considering that acid reactions have mainly been catalyzed by anionic POM clusters containing early transition metals (W, Mo, V, etc.) (*4*, *5*, *46*), using positively charged clusters with heavy main group elements and controlling the metal ion defects as in this study may open up possibilities in the design of solid-state catalysts. As there are many metal-oxo clusters containing Bi and Sb (*48*, *49*), they should also exhibit acidity by protonation via introducing defects.

It is noted that sodalites $[Al_6Si_6O_{24}]$ framework (*28*), uranium clusters $[\{(UO_2)O_2(OH)\}_{24}]^{24-}$ (*29*), and M_8P_{16} (M = Cu, Ni) in clathrate compounds AM_2P_4 (A = Sr, Ba) (*30*) have a structure with similar topology (truncated octahedron, 4^66^8) as the $[Sb_{24-\delta}O_{36}]$ cage in the outer shell of the **HSbO** clusters (fig. S6). In these compounds, this framework can be modified to yield, e.g., the inner space to be used as a reaction field (*50*). Likewise, our **HSbO** clusters could be structurally modified, for example, we may be able to synthesize antimony oxide cage structures with different topologies (*51*, *52*) and higher-order structures (*53*). In addition, dissolving and isolating **HSbO** clusters would permit the use of single clusters for homogeneous catalysis and a broader deployment as building blocks for various organic-inorganic composites. For example, if we

can introduce permanent porosity into **HSbO**-based polycation composites, then the catalytic activity would be greatly enhanced because the reactant molecules can access not only the **HSbO** clusters on the crystal surface but also all the **HSbO** clusters inside.

Recall that various functions have been explored in anionic POM clusters such as the Keggin and Wells-Dawson types by modifying the clusters themselves, e.g., through elemental substitution (*3*) and addition of organic functional groups (*54*), and by forming organic-inorganic complexes in combination with various cations (*1*). Such synthetic approaches should be possible in our Sb-based cluster system, which can adjust the acidity and introduce porosity to improve the acid catalytic properties or to add other functions such as proton conductivity. It would also be interesting to examine how the catalysis of **HSbOI** is altered by elemental substitution, e.g., halide substitution at the iodine sites. To this end, it is important to understand the reaction mechanism, including the condensation process during the cluster formation.

MATERIALS AND METHODS

Synthesis

The powder sample of **HSbOI** was prepared as follows: Sb_2O_3 (99.9%, Wako; 2.0 g, 6.86 mmol) was dissolved in a mixture of HI (Wako; 6.8 M, 15.6 ml) and water (10 ml) and was stirred for 1 hour at 75°C. Adding water (500 ml) to this solution resulted in the precipitation of an orange powder. The suspension was stirred at 75°C for 1 hour and then at 0°C for 1 hour. The resulting product was recovered by filtration, washed with filtrate, and dehydrated through drying at 100°C under vacuum.

Characterization

The specimen for TEM study was prepared by grinding the powder in anhydrous hexane and putting a few drops of the resulting suspension onto Cu grids covered with a holey carbon layer. The ED experiment was performed using a FEI Tecnai G2 microscope operated at 200 kV. Energy-dispersive x-ray spectroscopy was performed using a FEI Tecnai Osiris microscope (200 kV), equipped with a Super-X detector. High-resolution STEM images were acquired using a FEI Titan 80-300 "cubed" microscope (300 kV). A Gatan double-tilt vacuum transfer holder was used to prevent the oxidation of the sample. 3D-ED tomography was used for the structure solution. Reciprocal space was scanned over an angular range of 85°, resulting in 696 reflections that were used for refinement with 590 reflections being independent. The PETS software (*55*) was used for the 3D reconstruction of reciprocal space.

Powder XRD data were collected using a D8 ADVANCE diffractometer (Bruker AXS) with Cu-K_α radiation. High-resolution powder SXRD experiments were performed at RT using a Debye-Scherrer camera, installed at SPring-8 BL02B2 of the Japan Synchrotron Radiation Research Institute. The incident beams from the bending magnet were monochromatized to $\lambda = 0.42096(1)$ Å. Sieved powder samples (<32 μm) were loaded into a Pyrex capillary with an inner diameter of 0.2 mm. The sealed capillary was rotated during the measurement to reduce the effect of preferred orientation of the crystallites. Powder neutron diffraction (ND) data were collected at RT using the high-resolution powder diffractometer BT-1 ($\lambda = 1.54060$ Å) at the National Institute of Standards and Technology (NIST) Center for Neutron Research. The collected SXRD patterns were analyzed by the Rietveld method using RIETAN-FP program (*56*).

^{1}H MAS-NMR spectra were recorded on a home-built spectrometer (*57*), operating at 400.23 MHz with a 3.2-mm T3 probe (Varian) in a magnetic field of 9.4 T. Tetramethylsilane (TMS) was used for the external chemical shift reference. The ^{1}H spectra were acquired using a single-pulse sequence with background suppression and a RFDR pulse sequence. The typical acquisition delay was 3 s; the 90° and 180° pulse widths were 2.7 and 5.4 μs, respectively; and the MAS rate was 20 kHz. To study proton exchange behavior, the as-prepared samples were immersed in light or heavy water at 80°C overnight, followed by drying at RT.

N_2 (77 K) adsorption and water vapor sorption (288 to 303 K) isotherms were measured using a volumetric gas sorption apparatus BELSORP-mini II and BELSORP-max (MicrotracBEL Corp), respectively. Before the sorption measurements, the weighted sample (ca. 0.1 g) was ground and treated in vacuum at 373 K for 3 hours. Sorption equilibrium was determined on the basis of a pressure change of ±0.3% over 5 min, and the sorption enthalpies (ΔH_{abs}) were calculated using the Clausius-Clapeyron equation.

Thermogravimetry was measured under dry N_2 flow (100 ml min^{-1}) using a Thermo Plus 2 (Rigaku) thermogravimetric analyzer, with α-Al_2O_3 as a reference. The temperature was held at 30°C for 30 min, increased to 500°C with a heating rate of 10°C min^{-1}, and held at 500°C for 30 min.

Certain commercial equipment, instruments, or materials are identified in this document. Such identification does not imply recommendation or endorsement by the NIST, nor does it imply that the products identified are necessarily the best available for the purpose.

Catalytic reaction

Pinacol rearrangement and Barbier-Grignard reactions were carried out in a glass reactor equipped with a magnetic stirrer. In a typical run of pinacol rearrangement reaction, a mixture of pinacol (0.668 mmol), naphthalene (0.267 mmol, internal standard), and **HSbOI** (300 mg, 0.01 mmol) in toluene (2 ml) was stirred under air at 373 K. In a typical run of Barbier-Grignard reaction, a mixture of benzaldehyde (0.50 mmol), allyltributyltin (1.0 mmol), and **HSbOI** (15 or 30 mg, 0.5 or 1.0 μmol) in water (1 ml) was stirred under air at 353 K. After the reaction, 1,2-dimethoxybenzene was added to the reaction mixture as an internal standard. The reaction progress was followed by GC using a GC-2014 (Shimadzu) fitted with an InertCap 5 (pinacol rearrangement reaction) or TC-WAX (Barbier-Grignard reaction) capillary column (GL Sciences) and a flame ionization detector, and ^{1}H NMR measurements. TON and TOF was calculated from following equation; TON = [yield (%)]/[amount of catalyst (mol)/amount of substrate (mol)], TOF ($hour^{-1}$) = TON/reaction time (hours). For ICP-MS measurement (Agilent Technologies, Agilent 8800), 30.8 mg of **HSbOI** was dispersed in 1 ml of water, and the Barbier-Grignard reaction was carried out for 24 hours. The concentration of Sb in the reaction solution was 18 μg ml^{-1} or 0.4% of the catalyst added.

Computational methods

DFT computations for the large **HSbO** cluster were performed with the Gaussian 09 package. Calculations were carried out using the extended cluster of $[Sb_{36}O_{50}]^{8+}$ (and protonated $[HSb_{36}O_{50}]^{9+}$), which is composed of $[Sb_{34}O_{44}]$ from the **HSbO** cluster plus O—Sb (× 2) and O—V_{Sb} (× 4) from the $Sb_{6-\delta}I_8O_6$ cluster (where V_{Sb} represents an antimony vacancy).

For the outer shell of the **HSbO** cluster, a small deficiency (occupancy, $g \sim 0.95$) in Sb3 (Wyckoff site 96*j*) was ignored, while the three-split Sb2 sites (96*k*, $g \sim 0.31$) were placed at the ideal site (32*f*, $g = 1$), yielding $[Sb_{32}O_{36}]$. For the inner shell, reflecting the experimental defect ($g \sim 0.319$), we removed four of the six antimonies for Sb1 in $[Sb_6O_8]$, resulting in $[Sb_2O_8]$. Thus, outer $[Sb_{32}O_{36}]$ and inner $[Sb_2O_8]$ clusters are combined to give a $[Sb_{34}O_{44}]$ composition. Furthermore, the capping O4—Sb4 from $Sb_{6-\delta}I_8O_6$ was added on the square face of the **HSbO** truncated octahedron to account for the sizable interaction between the **HSbO** and $Sb_{6-\delta}I_8O_6$ (see section Structural features of clusters in **HSbOI**). In addition, the "capping" oxygen atoms of the $Sb_{6-\delta}I_8O_6$ cluster and the Sb atoms (Sb4) were combined into a $[Sb_{34}O_{44}]$ cluster, taking into account the large defect ($g \sim 0.351$) in the Sb4 site ([O—Sb] × 2, [O—V_{Sb}] × 4). The two [O—Sb] and the two Sb1 atoms are arranged vertically in Fig. 4B.

As shown in Fig. 4B, O atoms of the $Sb_{36}O_{50}$ cluster can be divided into three layers according to their distance from the center of the cluster. The O atoms of **HSbO** cluster can be classified into five groups and the capping O atoms into two groups (fig. S19). One proton is placed near any of the seven O atoms to form a $[HSb_{36}O_{50}]^{9+}$ cluster. The most stable orientation of the protons bound to each O atom was determined. 3D XYZ coordinates of each proton in the $[HSb_{36}O_{50}]^{9+}$ cluster were fully optimized using the B3LYP functional, while keeping the XYZ coordinates of the framework $Sb_{36}O_{50}$ cluster fixed. The basis sets are LanL2DZ for Sb atoms and cc-pVDZ for a proton and O atoms. The structure of TMS molecule was fully optimized without any geometric constraint in the B3LYP/cc-pVDZ level of theory.

Total energies and NMR properties were calculated using the B3LYP functional and triple-ζ basis set. The basis sets are LanL08 for Sb atoms and cc-pVTZ for proton and O atoms in the $[HSb_{36}O_{50}]^{9+}$ cluster, and cc-pVTZ for all the atoms included in the TMS molecule. The nuclear magnetic shielding tensors of the optimized $[HSb_{36}O_{50}]^{9+}$ clusters and the reference TMS molecule were computed by the GIAO method (*58*) implemented in the Gaussian09 package. Each isotropic chemical shift of proton in the $[HSb_{36}O_{50}]^{9+}$ cluster was calculated by setting the average of the computed NMR isotropic shielding constants of the H atoms in the TMS molecule as origin.

The 3D ESPs were made from the converged Kohn-Sham orbitals by the utility cubegen program of Gaussian 09 package. The bonding and lone-pair orbitals of $[Sb_{34}O_{44}]^{14+}$ clusters were also calculated by the aforementioned B3LYP functional and triple-ζ basis sets. This is the core part of the $[Sb_{36}O_{50}]^{8+}$ cluster in Fig. 4. The rendered wave function was analyzed by Gaussian Natural Bond Orbital version 3.1 (*59*) implemented in the Gaussian09 package. The obtained bonding and lone-pair orbitals were visualized by GaussView 5.0 package with the isovalue = 0.02, except for the isovalue = 0.1 used to show the lone-pair orbitals of the outer shell Sb atoms (Fig. 3 and fig. S20).

SUPPLEMENTARY MATERIALS

Supplementary material for this article is available at https://science.org/doi/10.1126/sciadv.abm5379

REFERENCES AND NOTES

1. A. Misra, K. Kozma, C. Streb, M. Nyman, Beyond charge balance: Counter-cations in polyoxometalate chemistry. *Angew. Chem. Int. Ed.* **59**, 596–612 (2020).
2. D. L. Long, E. Burkholder, L. Cronin, Polyoxometalate clusters, nanostructures and materials: From self assembly to designer materials and devices. *Chem. Soc. Rev.* **36**, 105–121 (2007).
3. M. Hutin, M. H. Rosnes, D. L. Long, L. Cronin, in *Comprehensive Inorganic Chemistry II*, J. Reedijk, K. Poeppelmeier, Eds. (Elsevier, ed. 2, 2013), pp. 241–269.
4. K. Kamata, K. Yonehara, Y. Sumida, K. Yamaguchi, S. Hikichi, N. Mizuno, Efficient epoxidation of olefins with ≥99% selectivity and use of hydrogen peroxide. *Science* **300**, 964–966 (2003).
5. I. A. Weinstock, R. E. Schreiber, R. Neumann, Dioxygen in polyoxometalate mediated reactions. *Chem. Rev.* **118**, 2680–2717 (2018).
6. S. Uchida, Frontiers and progress in cation-uptake and exchange chemistry of polyoxometalate-based compounds. *Chem. Sci.* **10**, 7670–7679 (2019).
7. J. T. Rhule, C. L. Hill, D. A. Judd, R. F. Schinazi, Polyoxometalates in medicine. *Chem. Rev.* **98**, 327–358 (1998).
8. J. M. Clemente-Juan, E. Coronado, A. Gaita-Arino, Magnetic polyoxometalates: From molecular magnetism to molecular spintronics and quantum computing. *Chem. Soc. Rev.* **41**, 7464–7478 (2012).
9. J.-H. Son, H. Choi, Y.-U. Kwon, Porous crystal formation from polyoxometalate building blocks: Single-crystal structure of $[AlO_4Al_{12}(OH)_{12}(H_2O)_{24}][Al(OH)_6Mo_6O_{18}]_2(OH)\cdot 29.5H_2O$. *J. Am. Chem. Soc.* **122**, 7432–7433 (2000).
10. P. Mialane, A. Dolbecq, L. Lisnard, A. Mallard, J. Marrot, F. Sécheresse, $[\varepsilon\text{–}PMo_{12}O_{36}(OH)_4\{La(H_2O)_4\}_4]^{5+}$: The first ε-$PMo_{12}O_{40}$ Keggin ion and its association with the two-electron-reduced α-$PMo_{12}O_{40}$ isomer. *Angew. Chem. Int. Ed.* **41**, 2398–2401 (2002).
11. Z. Mayerova, M. Johnsson, S. Lidin, Lone-pair interfaces that divide inorganic materials into ionic and covalent parts. *Angew. Chem. Int. Ed.* **45**, 5602–5606 (2006).
12. W. Wang, L. B. Fullmer, N. A. G. Bandeira, S. Goberna-Ferrón, L. N. Zakharov, C. Bo, D. A. Keszler, M. Nyman, Crystallizing elusive chromium polycations. *Chem* **1**, 887–901 (2016).
13. O. Sadeghi, L. N. Zakharov, M. Nyman, Aqueous formation and manipulation of the iron-oxo keggin ion. *Science* **347**, 1359–1362 (2015).
14. J. A. Sommers, D. C. Hutchison, N. P. Martin, K. Kozma, D. A. Keszler, M. Nyman, Peroxide-promoted disassembly reassembly of Zr-polyoxocations. *J. Am. Chem. Soc.* **141**, 16894–16902 (2019).
15. M. Shohel, J. L. Bjorklund, J. A. Smith, D. V. Kravchuk, S. E. Mason, T. Z. Forbes, Formation of nanoscale $[Ge_4O_{16}Al_{48}(OH)_{108}(H_2O)_{24}]^{20+}$ from condensation of ε-$GeAl_{12}^{8+}$ Keggin Polycations*. *Angew. Chem. Int. Ed.* **60**, 8755–8759 (2021).
16. G. Johansson, G. Lundgren, L. G. Sillén, R. Söderquist, On the crystal structure of a basic aluminium sulfate and the corresponding selenate. *Acta Chem. Scand.* **14**, 769–771 (1960).
17. M. Šimuneková, D. Prodius, V. Mereacre, P. Schwendt, C. Turta, M. Bettinelli, A. Speghini, Y. Lan, C. E. Anson, A. K. Powell, Tetradecanuclear lanthanide-vanadium "nanochocolates": Catalytically-active cationic heteropolyoxovanadium clusters. *RSC Adv.* **3**, 6299–6304 (2013).
18. J. A. Sommers, D. C. Hutchison, N. P. Martin, L. Palys, J. M. Amador, D. A. Keszler, M. Nyman, Differentiating Zr/Hf^{IV} aqueous polyoxocation chemistry with peroxide ligation. *Inorg. Chem.* **60**, 1631–1640 (2021).
19. K. Kozma, L. N. Zakharov, M. Nyman, Countercation-controlled nuclearity of Zr/Hf peroxo oxalates. *Cryst. Growth Des.* **20**, 6519–6527 (2020).
20. T. A. Stewart, D. E. Trudell, T. M. Alam, C. A. Ohlin, C. Lawler, W. H. Casey, S. Jett, M. Nyman, Enhanced water purification: A single atom makes a difference. *Environ. Sci. Technol.* **43**, 5416–5422 (2009).
21. A. F. Oliveri, C. A. Colla, C. K. Perkins, N. Akhavantabib, J. R. Callahan, C. D. Pilgrim, S. E. Smart, P. H. Y. Cheong, L. Pan, W. H. Casey, Isomerization of Keggin Al_{13} ions followed by diffusion rates. *Chem. A Eur. J.* **22**, 18682–18685 (2016).
22. W. Zhou, N. Ogiwara, Z. Weng, N. Tamai, C. Zhao, L.-K. Yan, S. Uchida, Isomeric effects on the acidity of Al_{13}Keggin clusters in porous ionic crystals. *Chem. Commun.* **57**, 8893–8896 (2021).
23. Z. Hugonin, M. Johnsson, S. Lidin, $Cu_{20}Sb_{35}O_{44}Br_{37}$ – One structure, two temperature dependencies. *Solid State Sci.* **10**, 160–167 (2008).
24. M. Edstrand, R. Brodersen, L. G. Sillén, A. Linnasalmi, P. Laukkanen, On the crystal structure of the antimony oxychloride $Sb_4O_5Cl_2$ and isomorphous oxybromide. *Acta Chem. Scand.* **1**, 178–203 (1947).
25. D. Batuk, M. Batuk, A. M. Abakumov, J. Hadermann, Synergy between transmission electron microscopy and powder diffraction: Application to modulated structures. *Acta Crystallogr. B* **71**, 127–143 (2015).
26. B. L. Nannenga, D. Shi, A. G. W. Leslie, T. Gonen, High-resolution structure determination by continuous-rotation data collection in MicroED. *Nat. Methods* **11**, 927–930 (2014).
27. J. Hadermann, A. M. Abakumov, Structure solution and refinement of metal-ion battery cathode materials using electron diffraction tomography. *Acta Crystallogr. B* **75**, 485–494 (2019).
28. I. Hassan, H. D. Grundy, The crystal structures of sodalite-group minerals. *Acta Crystallogr. B* **40**, 6–13 (1984).
29. O. Renier, C. Falaise, H. Neal, K. Kozma, M. Nyman, Closing uranyl polyoxometalate capsules with bismuth and lead polyoxocations. *Angew. Chem. Int. Ed.* **128**, 13678–13682 (2016).

30. J.-A. Dolyniuk, J. Wang, K. Lee, K. Kovnir, Twisted Kelvin cells and truncated octahedral cages in the crystal structures of unconventional clathrates, AM_2P_4 (A = Sr, Ba; M = Cu, Ni). *Chem. Mater.* **27**, 4476–4484 (2015).
31. J. C. Gabriel, K. Boubekeur, S. Uriel, P. Batail, Chemistry of hexanuclear rhenium chalcohalide clusters. *Chem. Rev.* **101**, 2037–2066 (2001).
32. F. Takeiri, T. Yajima, S. Hosokawa, Y. Matsushita, H. Kageyama, Topochemical anion insertion into one-dimensional Bi channels in Bi_2PdO_4. *J. Solid State Chem.* **286**, 121273 (2020).
33. K. Isobe, A. Yagasaki, Cubane-type clusters as potential models for inorganic solid surfaces. *Acc. Chem. Res.* **26**, 524–529 (1993).
34. A. E. Maughan, A. M. Ganose, M. M. Bordelon, E. M. Miller, D. O. Scanlon, J. R. Neilson, Defect tolerance to intolerance in the vacancy-ordered double perovskite semiconductors Cs_2SnI_6 and Cs_2TeI_6. *J. Am. Chem. Soc.* **138**, 8453–8464 (2016).
35. D. Freude, M. Hunger, H. Pfeifer, W. Schwieger, ^{1}H MAS NMR studies on the acidity of zeolites. *Chem. Phys. Lett.* **128**, 62–66 (1986).
36. F. Haase, J. Sauer, ^{1}H NMR chemical shifts of ammonia, methanol, and water molecules interacting with Broensted acid sites of zeolite catalysts: Ab-initio calculations. *J. Phys. Chem. C* **98**, 3083–3085 (1994).
37. H. Huo, L. Peng, Z. Gan, C. P. Grey, Solid-state MAS NMR studies of Brønsted acid sites in zeolite H-mordenite. *J. Am. Chem. Soc.* **134**, 9708–9720 (2012).
38. G. Ye, N. Janzen, G. R. Goward, Solid-state NMR study of two classic proton conducting polymers: Nafion and sulfonated poly(ether ether ketone)s. *Macromolecules* **39**, 3283–3290 (2006).
39. S. Uchida, K. Inumaru, M. Misono, States and dynamic behavior of protons and water molecules in $H_3PW_{12}O_{40}$ pseudoliquid phase analyzed by solid-state MAS NMR. *J. Phys. Chem. B* **104**, 8108–8115 (2000).
40. J. A. Berson, What is a discovery? Carbon skeletal rearrangements as counter-examples to the rule of minimal structural change. *Angew. Chem. Int. Ed.* **41**, 4655–4660 (2002).
41. B. Török, I. Bucsi, T. Beregszászi, I. Kapocsi, Á. Molnár, Transformation of diols in the presence of heteropoly acids under homogeneous and heterogeneous conditions. *J. Mol. Catal. A: Chemical* **107**, 305–311 (1996).
42. T. Okuhara, T. Nishimura, H. Watanabe, M. Misono, Insoluble heteropoly compounds as highly active catalysts for liquid-phase reactions. *J. Mol. Catal.* **74**, 247–256 (1992).
43. C.-J. Li, Aqueous Barbier-Grignard type reaction: Scope, mechanism, and synthetic applications. *Tetrahedron* **52**, 5643–5668 (1996).
44. M. Chen, C. Liang, F. Zhang, H. Li, Periodic mesoporous silica-supported scandium triflate as a robust and reusable Lewis acid catalyst for carbon–carbon coupling reactions in water. *ACS Sustain. Chem. Eng.* **2**, 486–492 (2013).
45. Y. Shimoyama, Z. Weng, N. Ogiwara, T. Kitao, Y. Kikukawa, S. Uchida, Isostructural mesoporous ionic crystals as a tunable platform for acid catalysis. *Dalton Trans.* **49**, 10328–10333 (2020).
46. H. Lv, Y. V. Geletii, C. Zhao, J. W. Vickers, G. Zhu, Z. Luo, J. Song, T. Lian, D. G. Musaev, C. L. Hill, Polyoxometalate water oxidation catalysts and the production of green fuel. *Chem. Soc. Rev.* **41**, 7572–7589 (2012).
47. J. Duan, M. Higuchi, J. Zheng, S.-i. Noro, I. Y. Chang, K. Hyeon-Deuk, S. Mathew, S. Kusaka, E. Sivaniah, R. Matsuda, S. Sakaki, S. Kitagawa, Density gradation of open metal sites in the mesospace of porous coordination polymers. *J. Am. Chem. Soc.* **139**, 11576–11583 (2017).
48. D. Mansfeld, L. Miersch, T. Rüffer, D. Schaarschmidt, H. Lang, T. Böhle, R. W. Troff, C. A. Schalley, J. Müller, M. Mehring, From $\{Bi_{22}O_{26}\}$ to chiral ligand-protected $\{Bi_{38}O_{45}\}$–based bismuth oxido clusters. *Chem. A Eur. J.* **17**, 14805–14810 (2011).
49. Z.-F. Wu, B. Hu, Z.-H. Fu, H. Wang, G. Xu, L.-K. Gong, G.-D. Zou, X.-Y. Huang, J. Li, $[Ba_{13}Sb_{36}Cl_{34}O_{54}]^{8-}$: High-nuclearity cluster for the assembly of nanocluster-based compounds. *Chem. Commun.* **55**, 7442–7445 (2019).
50. J. Wang, J.-A. Dolyniuk, K. Kovnir, Unconventional clathrates with transition metal–phosphorus frameworks. *Acc. Chem. Res.* **51**, 31–39 (2018).
51. B. Hu, M.-L. Feng, J.-R. Li, Q.-P. Lin, X.-Y. Huang, Lanthanide antimony oxohalides: From discrete nanoclusters to inorganic-organic hybrid chains and layers. *Angew. Chem. Int. Ed.* **50**, 8110–8113 (2011).
52. C. Falaise, M. Nyman, The key role of U_{28} in the aqueous self-assembly of uranyl peroxide nanocages. *Chem. A Eur. J.* **22**, 14678–14687 (2016).
53. P.-Q. Zheng, Y.-P. Ren, L.-S. Long, R.-B. Huang, L.-S. Zheng, pH-dependent assembly of Keggin-based supramolecular architecture. *Inorg. Chem.* **44**, 1190–1192 (2005).
54. M. Xu, H. Traustason, F. D. Bo, S. Hickam, S. Chong, L. Zhang, A. G. Oliver, P. C. Burns, Supramolecular assembly of geometrically unstable hybrid organic–inorganic uranyl peroxide cage clusters and their transformations. *J. Am. Chem. Soc.* **141**, 12780–12788 (2019).
55. L. Palatinus, P. Brazda, M. Jelinek, J. Hrda, G. Steciuk, M. Klementova, Specifics of the data processing of precession electron diffraction tomography data and their implementation in the program PETS2.0. *Acta Crystallogr. B* **75**, 512–522 (2019).
56. F. Izumi, K. Momma, Three-dimensional visualization in powder diffraction. *Solid State Phenom.* **130**, 15–20 (2007).
57. K. Takeda, OPENCORE NMR: Open-source core modules for implementing an integrated FPGA-based NMR spectrometer. *J. Magn. Reson.* **192**, 218–229 (2008).
58. K. Wolinski, J. F. Hinton, P. Pulay, Efficient implementation of the gauge-independent atomic orbital method for NMR chemical shift calculations. *J. Am. Chem. Soc.* **112**, 8251–8260 (1990).
59. A. E. Reed, F. Weinhold, Natural localized molecular orbitals. *J. Chem. Phys.* **83**, 1736–1740 (1985).
60. K. Momma, F. Izumi, VESTA 3 for three-dimensional visualization of crystal, volumetric and morphology data. *J. Appl. Cryst.* **44**, 1272–1276 (2011).

Acknowledgments: We thank NIST for support and use of neutron facilities. **Funding:** This work was partially supported by CREST (grant no. JPMJCR1421), JSPS KAKENHI (grant nos. JP16H06438, JP16H06439, JP16H06440, JP16K21724, JP17H06439, and JPJSCCA20200004), and JSPS Core-to-Core Program (JPJSCCA20200004). **Author contributions:** Y.W., T.Y., M.Y., M.H., O.T., D.K., J.X., T.G., and R.A. synthesized **HSbOI**. K.H.-D. and I.-Y.C carried out theoretical calculations. Y.N. and T.K. performed NMR measurements. T.Y. and C.M.B. measured ND. Y.W., T.Y., O.M.K., D.K. and C.T. analyzed x-ray and ND data. O.M.K., J.H., and A.M.A. performed TEM. Y.S., N.O., and S.U. conducted catalytic properties. Y.W. and H.K. wrote the manuscript, with comments from other authors. **Competing interests:** The authors declare that they have no competing interests. **Data and materials availability:** All data needed to evaluate the conclusions in the paper are present in the paper and/or the Supplementary Materials.

Submitted 23 September 2021
Accepted 4 May 2022
Published 17 June 2022
10.1126/sciadv.abm5379